ACS APPLIED MATERIALS & INTERFACES

Research Article

www.acsami.org

Nanosheet-Assembled $ZnFe_2O_4$ Hollow Microspheres for High-Sensitive Acetone Sensor

Xin Zhou, Xiaowei Li, Hongbin Sun, Peng Sun,* Xishuang Liang, Fengmin Liu, Xiaolong Hu, and Geyu Lu*

State Key Laboratory on Integrated Optoelectronics, College of Electronic Science and Engineering, Jilin University, Changchun 130012, People's Republic of China

Supporting Information

ABSTRACT: Semiconductor oxides with hierarchically hollow architecture can provide significant advantages as sensing materials for gas sensors by facilitating the diffusion of target gases. Herein, we develop a facile template-free solvothermal strategy combined with the subsequent thermal treatment process toward the successful synthesis of novel $ZnFe_2O_4$ hollow flower-like microspheres. The images of electron microscopy unambiguously indicated that the $ZnFe_2O_4$ nanosheets with thickness of around 20 nm assembled hierarchically to form the unique flower-like architecture. As a proof-of-concept demonstration of the function, the as-prepared product was utilized as sensing material for gas sensor. Significantly, in virtue of the porous shell structure, hollow interior, and large surface area, $ZnFe_2O_4$ hierarchical microspheres exhibited high response, excellent cyclability, and long-term stability to acetone at the operating temperature of 215 °C.

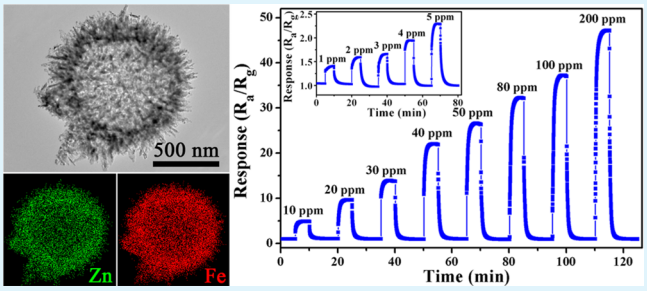

KEYWORDS: *hierarchical structure, $ZnFe_2O_4$, solvothermal method, acetone, sensor*

1. INTRODUCTION

Because of the outstanding characteristics of easy manufacture, low power consumption, and cost, gas sensors are regarded as one of the effective approaches to the detection of toxic, harmful, flammable, and explosive gases. The basic working principle for oxide semiconductors gas sensors such as α-Fe_2O_3,[1,2] ZnO,[3,4] SnO_2,[5−8] In_2O_3,[9,10] WO_3[11,12] (n-type) and Co_3O_4,[13,14] NiO[15,16] (p-type), et al.,[17] is that the interactions between the surface adsorbed oxygen species and target gases lead to a remarkable change in the resistance. Therefore, the composition, crystalline size, surface morphology, and microstructure of oxide semiconductors play essential roles in determining the sensing properties. In recent years, three-dimensional hierarchical architectures comprised of many low dimensional nanobuilding blocks with controlled size, shape, composition, and internal structure have received tremendous interest, as these structures are expected to provide more handles to tailor the properties for different applications.[18,19] On this point, rational design of hierarchical sensing materials with novel architectures will be increasingly important in the construction of high performance gas sensors. Because of the large specific surface area, well-defined interior voids, low density, and good surface permeability, oxide semiconductors with hierarchically hollow structures provide substantial performance boosts in gas sensors.[20,21] In general, the manipulation of hollow materials is carried out by template-directed preparation. However, this kind of synthetic strategy is quite costly, tedious, and low yield.[22−24] Moreover, template contamination mostly decreased the activity of synthesized materials. To avoid complicated operations, a number of template-free routes have been devised for preparing hierarchically hollow microstructures and nanostructures.[25−28] Despite that intense efforts have been dedicated, it is still of huge challenge but desirable to develop a facile, reliable, and scalable route for the rational synthesis of hollow microstructures.

As one kind of important functional materials, spinel $ZnFe_2O_4$ has been widely investigated in many fields.[29−32] However, $ZnFe_2O_4$ has been commonly utilized as anode material in lithium-ion batteries over the last few decades.[29,33] By contrast, there is little literature on its sensing behaviors. Furthermore, among the literature about its sensing behaviors, most of them are low-dimensional nanostructures.[34−36] In this regard, the design and synthesis of $ZnFe_2O_4$ with unique microstructures and expanding its potential application in gas sensors still have importantly scientific and practical significance. Nevertheless, to the best of our knowledge, the facile synthesis of hollow $ZnFe_2O_4$ flower-like microspheres via a facile solvothermal method without any help of templates is rarely reported.

In the present work, a simple solvothermal route combined with the subsequent annealing process was devised for the preparation of hierarchical $ZnFe_2O_4$ hollow microspheres,

Received: April 23, 2015
Accepted: June 23, 2015
Published: June 23, 2015

DOI: 10.1021/acsami.5b03537
ACS Appl. Mater. Interfaces 2015, 7, 15414−15421

comprised of many nanosheets with thickness of approximately 20 nm as the primary building blocks. Moreover, gas sensors based on the as-obtained product were fabricated, and their gas sensing performances were investigated. It was revealed that hierarchical $ZnFe_2O_4$ microsphere-based sensor device exhibited high response, good selectivity, and long-term stability to acetone at the optimum operating temperature of 215 °C.

2. EXPERIMENTAL SECTION

2.1. Preparation of $ZnFe_2O_4$ Hollow Microspheres. All of the chemical reagents used in the experiment were analytical grade as purchased from Sinopharm Chemical Reagent Co. Ltd. of China, and directly used without any further purification. A typical synthesis procedure of hollow $ZnFe_2O_4$ flower-like microspheres was conducted as follows: 0.5 mmol of $Zn(CH_3COO)_2{\cdot}2H_2O$ and 1 mmol of $Fe(NO_3)_3{\cdot}9H_2O$ were completely dissolved into a mixed solvent of 8 mL of glycerol and 30 mL of isopropanol under continuous magnetic stirring. After being stirred for several minutes, the homogeneous solution was transformed into a 40 mL Teflon-lined stainless steel autoclave, which was then tightly sealed and maintained at 180 °C for 12 h in an electric oven. Subsequently, the autoclave was allowed to cool to room temperature naturally, and the precipitate was collected by centrifugation and washed several times with deionized water and ethanol alternately, then dried in air at 80 °C for 12 h. Finally, the as-prepared intermediate product was transformed into $ZnFe_2O_4$ by calcination at 400 °C for 2 h under air atmosphere with a heating rate of 2 °C/min.

2.2. Materials Characterization. The powder X-ray diffraction (XRD) patterns were performed on a Rigaku D/Max-2550 V X-ray diffractometer using high-intensity Cu Kα radiation (λ = 1.5406 Å) in the range of 10°−70° (2θ) to investigate the crystallographic phases of the as-prepared sample. The surface morphology and microstructure of the products were directly observed by field emission scanning electron microscopy (FESEM) observation, which was carried out with a JEOL JSM-7500F microscope operated at an accelerating voltage of 15 kV. Transmission electron microscopy (TEM) and high-resolution transmission electron microscopy (HRTEM) images were taken on a JEOL JSM-2100F microscope operated at an accelerating voltage of 200 kV. The chemical compositions of the as-obtained sample were studied by energy dispersive X-ray spectrometry (EDS), which was measured by the TEM attachment. X-ray photoelectron spectroscopy (XPS) measurements were conducted on a Scienta ESCA200 spectrometer equipped with Al Kα radiation source. The specific surface area was estimated by the Brunauer−Emmett−Teller (BET) equation based on the nitrogen adsorption isotherm, which was measured with a Micromeritics Gemini VII apparatus (Surface Area and Porosity System) with prior degassing of the product under vacuum at 120 °C overnight.

2.3. Fabrication and Measurement of Gas Sensor. The fabrication process of the sensor device can be described as follows: first, an appropriate amount of the as-synthesized $ZnFe_2O_4$ hollow flowers was fully mixed with deionized water to prepare the homogeneous slurry, which was then coated onto an alumina tube by the assistance of a small brush to form a thick sensing film. The alumina tube is about 4 mm in length, 1.2 mm in external diameter, and 0.8 mm in internal diameter; besides, a pair of Au electrodes were installed at the end of the tube, and each electrode was connected with a pair of Pt wires. After drying in air at room temperature, the device was calcined at 400 °C for 2 h to improve its stability and repeatability. A Ni−Cr alloy coil then was inserted into the alumina tube as a heater, allowing us to control the operating temperature of the sensor by tuning the heating current. Finally, the sensor was constructed by connecting the corresponding junctions to the socket of sensor. The structure of the sensor is schematically illustrated in Figure S1 of the Supporting Information. The gas sensing performances of the as-fabricated gas sensor were evaluated by a static process, which was described detailedly in our previous work.[37] The sensor response was defined as $S = R_a/R_g$ for reducing gases or R_g/R_a for oxidizing gases, where R_a and R_g are the resistances measured in air and the test gas atmosphere, respectively. The time taken by the resistance to change from R_a to R_a−90% ($R_a - R_g$) was defined as the response time (τ_{res}), when the sensor was exposed to the test gas. On the contrary, when the sensor was retrieved from the test gas, the time taken by the resistance to range from R_g to R_g+90% ($R_a - R_g$) was defined as the recovery time (τ_{recov}).

3. RESULTS AND DISCUSSION

3.1. Structural and Morphological Characteristics. The original precursor directly obtained after the solvothermal reaction could be ZnFe-glycolate, as indicated by the X-ray diffraction (XRD) pattern exhibited in Figure S2 (Supporting Information), from which the especially strong diffraction peak located in the low-angle region (around 11°) was regarded as the representative characteristic of metal glycolates.[38−40] The morphology and microstructure of the precursor were studied by field emission scanning electron microscopy (FESEM). Figure S3 (Supporting Information) shows FESEM images of the precipitates with different magnifications. The panoramic FESEM image exhibited in Supporting Information Figure S3a clearly revealed that the product was entirely composed of large amounts of well-dispersed spherical microstructures. The magnified FESEM image presented in Supporting Information Figure S3b demonstrates that the diameters of these microspheres were around 1.1−1.3 μm. A close-up FESEM micrograph of an individual microsphere (Supporting Information Figure S3c) shows that the ZnFe-glycolate microspheres possessed quite rough surfaces, which were built up from numerous densely packed irregular shaped sheet-like subunits. More noticeably, a representative cracked microsphere shown in Supporting Information Figure S3d fairly brought to light the hollow interior of the as-obtained precursor from the broken part.

After the presynthesized ZnFe-glycolate precursor was annealed at 400 °C for 2 h under air atmosphere, the crystallographic structure of the product obtained after the calcination process was analyzed by X-ray diffraction (XRD) as shown in Figure 1. All of the diffraction peaks in this pattern

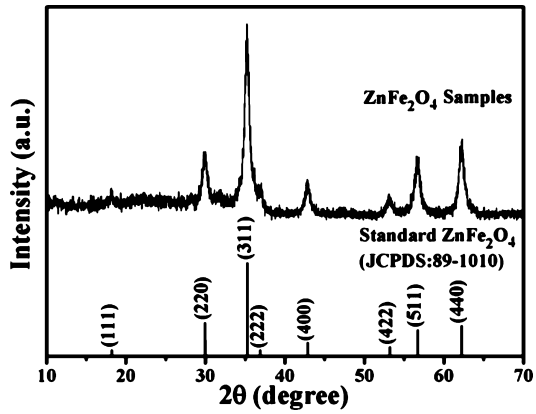

Figure 1. XRD pattern of the $ZnFe_2O_4$ sample obtained after calcining the ZnFe-glycolate precursor at 400 °C for 2 h.

could be perfectly indexed to the cubic spinel structure of $ZnFe_2O_4$ with lattice constant of a = 8.429 Å, which are consistent with those from the standard JCPDS card no. 89-1010. No residues or contaminants of the precursor compounds had been detected, indicating the complete formation of pure $ZnFe_2O_4$.

DOI: 10.1021/acsami.5b03537
ACS Appl. Mater. Interfaces 2015, 7, 15414−15421

The morphological and structural information on the as-obtained $ZnFe_2O_4$ sample after thermal treatment were further characterized by FESEM. A panoramic view of the product exhibited in Figure S4 (Supporting Information) clearly revealed that the calcined products were constructed by a large quantity of well-dispersed microspheres with sizes of 0.9−1.1 μm, which were slight smaller than that for the precursor (1.1−1.3 μm) due to the inward shrinkage during the transformation from ZnFe-glycolate to $ZnFe_2O_4$. The detailed morphology of the as-obtained $ZnFe_2O_4$ microspheres was provided by an enlarged FESEM image as shown in Figure 2a−c. Very interestingly, it is apparent to observe that the microstructure of $ZnFe_2O_4$ sample had perfectly inherited the hierarchical morphology of the corresponding flower-like ZnFe-glycolate microsphere even after the heat treatment, which was assembled by a large scale of closely interconnected nanosized sheets as primary building blocks. The obvious spaces between the neighboring nanosheets could be clearly discerned, and the mean thickness of these nanosheets was estimated to be approximately 20 nm from the higher magnification FESEM image of the surface of an individual microsphere, which is presented in Figure 2b. A representative FESEM image of a broken $ZnFe_2O_4$ microsphere depicted in Figure 2c further confirmed that the hollow cavity was well-maintained without any collapse.

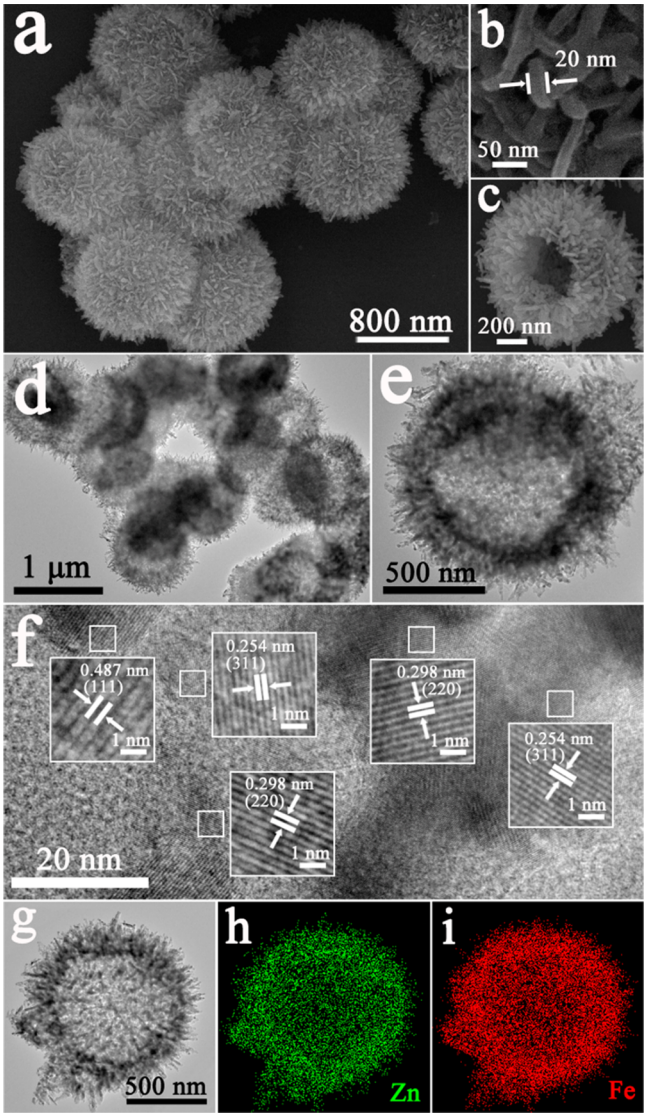

Figure 2. (a−c) Typical FESEM images of the hierarchical $ZnFe_2O_4$ microspheres with different magnifications. (d and e) TEM images of the hollow $ZnFe_2O_4$ microspheres. (f) HRTEM image. (g and h,i) TEM image of an individual microsphere and the corresponding elemental mapping images.

TEM observations were also conducted to provide insight into more detailed structural features of the flower-like $ZnFe_2O_4$ microspheres. Figure 2d displays a low magnification TEM image of the as-prepared sample, which illustrated that the product was made up of numerous microspheres with sizes of 0.8−1.1 μm. The hollow interior of these $ZnFe_2O_4$ flower-like microspheres could also be clearly identified by the sharp contrast between the dark edge and the pale center in the TEM image of an individual $ZnFe_2O_4$ microsphere (Figure 2e). Furthermore, a close-up view of the well-defined shell revealed that plenty of nanoscaled subunits (which are proved to be nanosheets from the FESEM observations) grew together with the hollow void as the center and congregated with each other to form the flower-like $ZnFe_2O_4$ architectures. High-resolution transmission electron microscopy (HRTEM) measurement was applied to supply the internal microstructure information on the as-prepared $ZnFe_2O_4$ hollow spheres. The lattice fringes could be apparently observed from Figure 2f, and constant values of the interplanar spacing between the adjacent lattice fringes were 0.487, 0.298, and 0.254 nm, which are consistent with (111), (220), and (311) planes of spinel $ZnFe_2O_4$, respectively. TEM elemental mapping was also conducted to study the elemental distribution in the hierarchical flower-like architecture. The elemental maps corresponding to a single flower-like $ZnFe_2O_4$ hollow microsphere (Figure 2g) shown in Figure 2h and i unambiguously confirmed the coexistence and homogeneous dispersion of Zn and Fe elements within the hollow flower-like microsphere. In addition, careful observation to Figure 2h and i indicated that whether for Zn or Fe, the elemental spatial distribution in the middle region was slightly less than that in the edge region, which further confirmed the hollow interior of the $ZnFe_2O_4$ flower-like microsphere.

X-ray photoelectron spectra (XPS) characterization was also performed to reveal the surface chemical composition and electronic states of the elements of the hollow $ZnFe_2O_4$ microstructure, and the corresponding results are presented in Figure 3. All of the binding energies in the XPS analysis are corrected for specimen charging by reflecting them to the C 1s peak (set at 284.6 eV). Two fitting peaks with binding energy values of ∼1045.0 and ∼1022.0 eV exhibited in the Zn 2p spectrum (Figure 3a) could be attributed to Zn $2p_{1/2}$ and Zn $2p_{3/2}$, respectively, indicating the Zn(II) oxidation state of $ZnFe_2O_4$. In terms of the Fe 2p spectrum (exhibited in Figure 3b), the binding energy peaks for Fe $2p_{3/2}$ at ∼713.6 and ∼711.5 eV correspond well with the tetrahedral site (A site) and octahedral site (B site), respectively. In addition, other peaks at binding energies of ∼725.6 and ∼719.5 eV are well consistent with the Fe $2p_{1/2}$ and the shakeup satellite structure, respectively. All of the above analyses confirmed the Fe(III) oxidation state in the $ZnFe_2O_4$ sample, which are in good accordance with reported literature.[41−43] Furthermore, the high-resolution O 1s spectra displayed in Figure 3c present a broad asymmetric curve, which can be fitted by two peaks with binding energies at ∼532.2 and ∼530.6 eV. It was widely acknowledged that the peak at ∼530.6 eV could be assigned to

DOI: 10.1021/acsami.5b03537
ACS Appl. Mater. Interfaces 2015, 7, 15414−15421

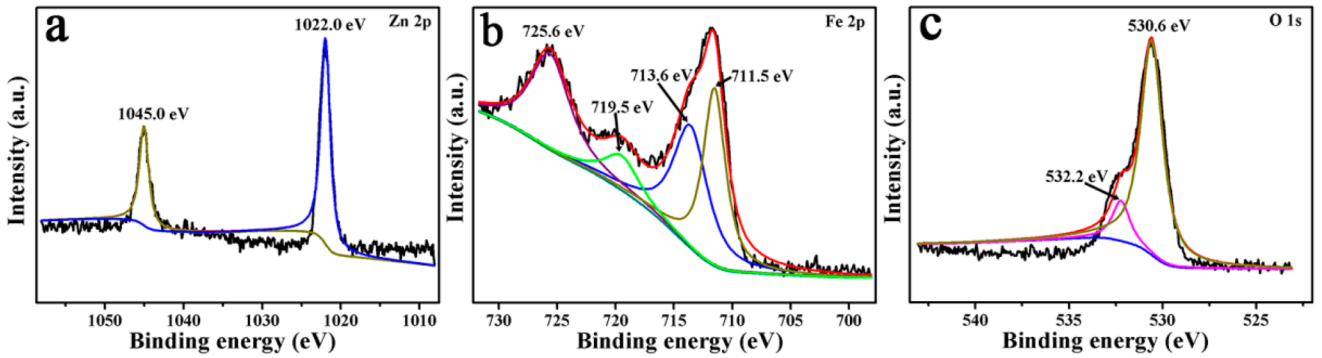

Figure 3. XPS survey spectra and fitted data of the as-obtained $ZnFe_2O_4$ microsphere: (a) Zn 2p, (b) Fe 2p, and (c) O 1s.

typical surface lattice oxygen and the other peak sitting at 532.2 eV is the characteristic of surface absorbed oxygen species such as $O_2^-{}_{ads}$ and $O^-{}_{ads}$.[44,45] The surface absorbed oxygen species play a positive role in the enhancement of gas sensing performances as they are capable of reacting with test gas molecules.[46]

Generally speaking, surface area is one of the most significant parameters to understand the behavior of a functional material, because the material reacts with its surroundings mainly via its surface, and a large surface area is more likely to adsorb more molecules, thus leading to the improved performances. Consequently, the specific surface area and the porosity of the as-prepared $ZnFe_2O_4$ product were evaluated by the nitrogen adsorption−desorption measurements. The representative N_2 adsorption−desorption isotherm and the corresponding BJH pore size distribution plot of the hollow $ZnFe_2O_4$ microstructure are given in Figure 4 and the inset. According to

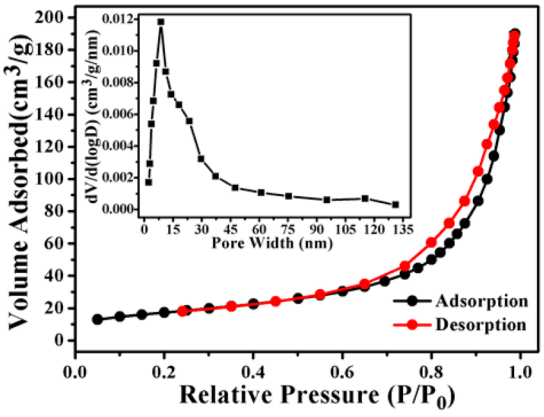

Figure 4. Nitrogen adsorption−desorption isotherm and corresponding BJH pore size distribution (inset) of the hollow $ZnFe_2O_4$ spherical architecture.

the International Union of Pure and Applied Chemistry (IUPAC) classification, the observed loop could be classified as type IV isotherm with a type H3 hysteresis loop,[47] implying the existence of mesopores in the material, and such a hollow flower-like structure gave rise to a high BET surface area of 66.7 m^2/g. The BJH pore size distribution (inset in Figure 4) calculated from adsorption branches demonstrated the pore size in $ZnFe_2O_4$ product was mainly concentrated in the 2−50 nm range, which might be attributed to the decomposition of organic agents that existed in the ZnFe-glycolate precursor during the calcination process. The high specific surface area and identified porosity are supposed to be really favorable for the construction of a high performance sensor device.

3.2. Gas Sensing Properties. To explore the advantages of the hierarchical $ZnFe_2O_4$ hollow flower-like microspheres, the as-prepared product was evaluated as sensing material to study its gas sensing properties. It is widely acknowledged that the operating temperature plays a crucial role in determining the sensing behavior of a sensor device; therefore, the response of the hierarchical $ZnFe_2O_4$-based sensor to 20 ppm acetone was first measured at 125−300 °C to elucidate the relationship between operating temperature and the gas response, the corresponding results of which are summarized in Figure 5a. It can be clearly observed that the acetone response first increased with working temperature, reached the maximum value of about 11.3 at 200 °C, and then gradually decreased, thus showing a "volcano" shape. The "increase-maximum-decrease" tendency can be explained as follows: at a low temperature, the test gas molecules are not activated enough to overcome the activation energy barrier to react with the surface absorbed oxygen species, leading to a relatively low response. Along with the increasing of temperature, both the higher reaction activity and the conversion of surface absorbed oxygen species ($O_{2(ads)} \rightarrow O_2^-{}_{(ads)} \rightarrow O^-{}_{(ads)} \rightarrow O^{2-}{}_{(ads)}$) contributed greatly to the higher response. At temperatures that are too high, the difficulty in gas adsorption causes the low utilization rate of the sensing material, resulting in the gas response decreasing.[48−50] However, not only high response, but also fast recovery speed should be paid attention to, on account of their vital role in avoiding possible loss and disasters for the practical application of a sensor device. Figure 5b exhibits the correlations between the response time (τ_{res}, black plot) and recovery time (τ_{recov}, red plot) versus operating temperature. Apparently, both response time and recovery time decreased along with the increasing working temperature. More noticeably, although the response to 20 ppm acetone at the operating temperature of 215 °C (S = 9.8) was slightly lower than that at 200 °C (S = 11.3), the recovery speed at 215 °C (τ_{recov} = 200 s) was much faster than that at 200 °C (τ_{recov} = 407 s). Accordingly, taking both gas response and recovery speed into consideration, we chose 215 °C as the optimum operating temperature of the hollow $ZnFe_2O_4$-based gas sensor, which was applied in all investigations hereinafter.

Because selectivity is a remarkable aspect of sensing properties, consequently, the responses of the as-fabricated gas sensor to various kinds of test gases (such as acetone, ethanol, methanol, formaldehyde, and so on) were investigated at different operating temperatures, the results of which were summarized in Figure 5c. The bar graph shown in Figure 5c

DOI: 10.1021/acsami.5b03537
ACS Appl. Mater. Interfaces 2015, 7, 15414−15421

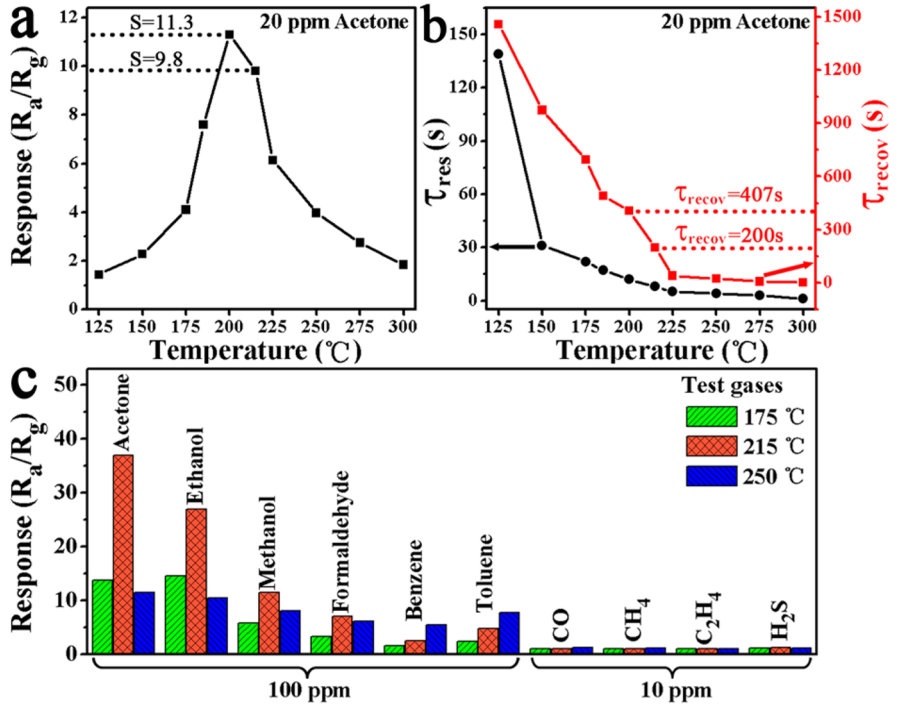

Figure 5. (a) Correlation between gas response to 20 ppm acetone and the operating temperature for the sensor fabricated from the as-obtained $ZnFe_2O_4$ microspheres. (b) Plots of response time (black plot) and recovery time (red plot) versus operating temperature. (c) Responses of the sensor to different test gases at various working temperatures.

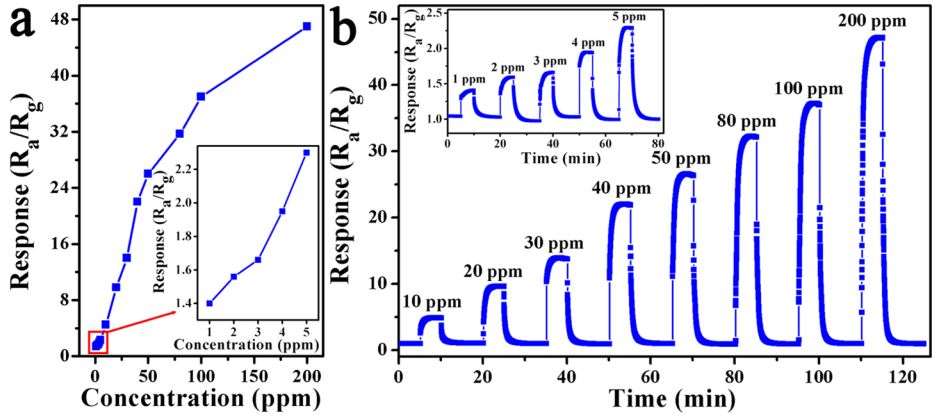

Figure 6. (a) Responses versus acetone concentration for $ZnFe_2O_4$-based gas sensor at 215 °C. (b) Dynamic response transient of the gas sensor to different concentrations of acetone at 215 °C. The insets of (a) and (b) show the response values and dynamic response curve versus acetone concentration in the range of 1−5 ppm, respectively.

demonstrated that the gas sensor put up ragged responses to these test gases at different operating temperatures, and it was also revealed that the selectivity changed along with working temperature. The variation in selectivity could be ascribed to the different values of the lowest unoccupied molecule orbit energy for gas molecules.[51] Significantly, the sensor device fabricated from hollow $ZnFe_2O_4$ microspheres displayed a much higher response and better selectivity to acetone as opposed to any other test gases at the working temperature of 215 °C.

The responses of the gas sensor changes along with the acetone concentrations were investigated at its optimum operating temperature (presented in Figure 6). It is evident that the response values increased sharply at relatively low acetone concentration, then the increase tendency slowed, and finally the rising tendency increased extremely slowly with further increase of the acetone concentration, indicating the sensor became more or less saturated (shown in Figure 6a). A plausible explanation for this situation can be summarized as follows: for low acetone concentration, a very weak surface reaction will occur due to the lower coverage of gas molecules on the material surface. An increase in acetone concentration makes the increasing of surface reactions, leading to the remarkable increase in gas response. With the acetone concentration further increased, the surface becomes gradually completely covered, resulting in the sensor response becomes more or less saturated just as we observed. Figure 6b presents the dynamic response-recovery transient of the sensor in the acetone concentration range from 1 to 200 ppm at the optimum operating temperature of 215 °C. It is apparent to see that the response curve displayed a stepwise distribution by orderly exposing the sensor device to different concentrations

DOI: 10.1021/acsami.5b03537
ACS Appl. Mater. Interfaces 2015, 7, 15414−15421

of acetone, which was in accordance with the results shown in Figure 6a. Significantly, the as-fabricated sensor device still showed response to acetone even when the acetone concentration was as low as 1 ppm, indicating the low detection limit to acetone (the inset of Figure 6b). Generally speaking, the working principle of semiconducting oxides gas sensor involves the receptor function, transducer function, and the utility factor of the sensing body.[52] The fascinating sensing performances observed here are likely to be ascribed to the unique architecture. In the flower-like hierarchical structure, the size of the nanosheets reaches a scale comparable with the electron depletion layer thickness, and thus complete depletion (transducer function) will be achieved.[53] Moreover, the hollow interiors and interspaces between the nansheets can facilitate the diffusion of test gases (utility factor) and improve the kinetics of the reaction of the test gas molecules with surface adsorbed oxygen species.

It is well-known that the long-term stability is one of the most important parameters for sensor devices from the perspective of practical application. As illustrated in Figure 7a,

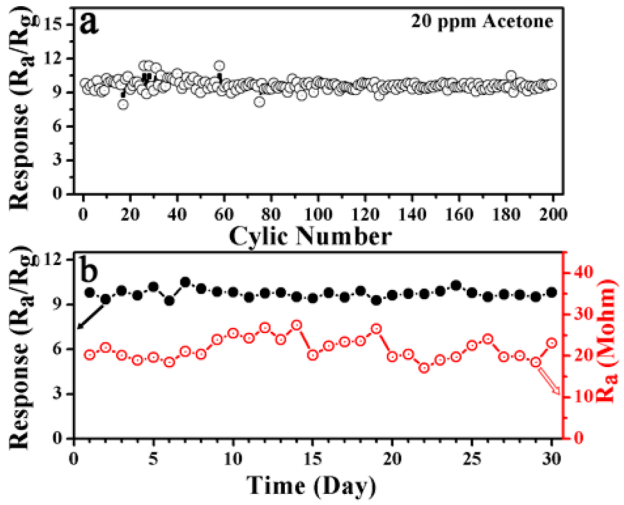

Figure 7. (a) Acetone response versus cycle number of the gas sensor evaluated at the optimum operating temperature of 215 °C. (b) Long-term stability of the gas sensor based on the as-prepared sample measured at the operating temperature of 215 °C.

cycling performance of the sensor response to 20 ppm acetone at 215 °C demonstrated the gas response could be well retained, which suggested that the hierarchical $ZnFe_2O_4$ spherical microstructure had superb robustness. In addition, the continuous measurement of the sensor response to 20 ppm acetone and the resistance in air atmosphere (R_a) during about 1 month further verified the sensor possesses splendid long-term stability (shown in Figure 7b).

3.3. Gas Sensing Mechanism. As a typical n-type semiconductor oxide, the popular and most accepted sensing mechanism for $ZnFe_2O_4$ belongs to the surface controlled model, which is based on resistance change of the semiconductor that is mainly caused by the adsorption and desorption process while exposed to different gas surroundings.[31,35,54,55] In air atmosphere, oxygen molecules (O_2) would adsorb on the surfaces of the $ZnFe_2O_4$ hollow sphere and capture free electrons from the conduction band to form surface adsorbed oxygen species ($O_{2(ads)}$, $O_2^-{}_{(ads)}$, $O^-{}_{(ads)}$, $O^{2-}{}_{(ads)}$). Consequently, a thick electron depletion layer and a relative high potential barrier formed on the surface region of $ZnFe_2O_4$, which would hinder the free electrons further trapped by the oxygen molecules, resulting in the sensor device showing relative high resistance (Figure 8a). In the presence of reducing

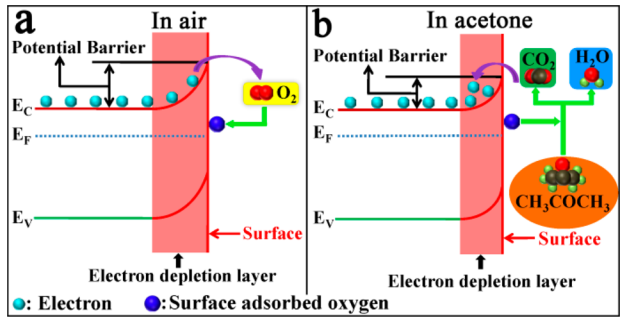

Figure 8. (a and b) Schematic illustration of acetone sensing mechanism for hollow $ZnFe_2O_4$ microspheres.

gases (like acetone, ethanol), these gas molecules would take part in the reaction with the former absorbed oxygen species and make the captured electrons release back to the conduction band of $ZnFe_2O_4$, giving rise to the thickness of the electron depletion layer and the height of the potential barrier both decreasing and lowering the resistance of the sensor (Figure 8b).

4. CONCLUSION

In summary, a facile solution-based strategy combined with the subsequent thermal-treatment process was employed for the successful preparation of hollow $ZnFe_2O_4$ flower-like microspheres, which were assembled by a large quantity of interconnected nanosheets as primary building blocks. When evaluated as sensing material for the potential sensing application, these novel $ZnFe_2O_4$ hollow architectures exhibited ultrahigh response and excellent long-term stability to acetone at the working temperature of 215 °C.

■ ASSOCIATED CONTENT

Ⓢ Supporting Information

Schematic diagram of the sensor device, XRD pattern of the ZnFe-glycolate precursor, typical FESEM images of the as-prepared ZnFe-glycolate precursor with different magnifications, and panoramic FESEM image of the $ZnFe_2O_4$ product. The Supporting Information is available free of charge on the ACS Publications website at DOI: 10.1021/acsami.5b03537.

■ AUTHOR INFORMATION

Corresponding Authors

*E-mail: spmaster2008@163.com.

*Tel.: +86 431 85167808. Fax: +86 431 85167808. E-mail: lugy@jlu.edu.cn.

Notes

The authors declare no competing financial interest.

■ ACKNOWLEDGMENTS

This work is supported by the National Nature Science Foundation of China (nos. 61374218, 61134010, and 61327804), the Program for Chang Jiang Scholars and Innovative Research Team in University (no. IRT13018), the National High-Tech Research and Development Program of China (863 Program, nos. 2013AA030902 and

DOI: 10.1021/acsami.5b03537
ACS Appl. Mater. Interfaces 2015, 7, 15414−15421

2014AA06A505), and Project 2015094 Supported by the Graduate Innovation Fund of Jilin University.

ABBREVIATIONS

XRD, X-ray diffraction
FESEM, field emission scanning electron microscopy
TEM, transmission electron microscopy
HRTEM, high-resolution transmission electron microscopy
EDS, energy dispersive X-ray spectrometry
XPS, X-ray photoelectron spectroscopy
BET, Brunauer–Emmett–Teller

REFERENCES

(1) Agarwala, S.; Lim, Z. H.; Nicholson, E.; Ho, G. W. Probing the Morphology-Device Relation of Fe_2O_3 Nanostructures towards Photovoltaic and Sensing Applications. *Nanoscale* **2012**, *4*, 194–205.
(2) Sun, Z. Y.; Yuan, H. Q.; Liu, Z. M.; Han, B. X.; Zhang, X. R. A Highly Efficient Chemical Sensor Material for H_2S: α-Fe_2O_3 Nanotubes Fabricated Using Carbon Nanotube Templates. *Adv. Mater.* **2005**, *17*, 2993–2997.
(3) Tamaekong, N.; Liewhiran, C.; Wisitoraat, A.; Phanichphant, S. Flame-Spray-Made Undoped Zinc Oxide Films for Gas Sensing Applications. *Sensors* **2010**, *10*, 7863–7873.
(4) Li, X. W.; Zhou, X.; Guo, H.; Wang, C.; Liu, J. Y.; Sun, P.; Liu, F. M.; Lu, G. Y. Design of Au@ZnO Yolk-Shell Nanospheres with Enhanced Gas Sensing Properties. *ACS Appl. Mater. Interfaces* **2014**, *6*, 18661–18667.
(5) Renard, L.; Brotz, J.; Fuess, H.; Gurlo, A.; Riedel, R. Hybrid Organotin and Tin Oxide-based Thin Films Processed from Alkynylorganotins: Synthesis, Characterization, and Gas Sensing Properties. *ACS Appl. Mater. Interfaces* **2014**, *6*, 17093–17101.
(6) Rwnard, L.; Babot, O.; Saadaoui, H.; Fuess, H.; Brota, J.; Gurlo, A.; Arveux, E.; Klein, A.; Toupance, T. Nanoscaled Tin Dioxide Films Processed from Organotin-Based Hybrid Materials: An Organometallic Route Toward Metal Oxide Gas Sensors. *Nanoscale* **2012**, *4*, 6806–6813.
(7) Singkammo, S.; Wisitsoraat, A.; Sriprachuabwong, C.; Tuantranont, A.; Phanichphant, S.; Liewhiran, C. Electrolytically Exfoliated Graphene-Loaded Flame-Made Ni-Doped SnO_2 Composite Film for Acetone Sensing. *ACS Appl. Mater. Interfaces* **2015**, *7*, 3077–3092.
(8) Punginsang, M.; Wisitsora-at, A.; Tuantranont, A.; Phanichphant, S.; Liewhiran, C. Effects of Cobalt Doping on Nitric Oxide, Acetone and Ethanol Sensing Performances of FSP-Made SnO_2 Nanoparticles. *Sens. Actuators, B* **2015**, *210*, 589–601.
(9) Sun, X. H.; Hao, H. R.; Ji, H. M.; Li, X. L.; Cai, S.; Zheng, C. M. Nanocasting Synthesis of In_2O_3 with Appropriate Mesostructured Ordering and Enhanced Gas-Sensing Property. *ACS Appl. Mater. Interfaces* **2014**, *6*, 401–409.
(10) Inyawilert, K.; Wisitsora-at, A.; Tuantranont, A.; Singjai, P.; Phanichphant, S.; Liewhiran, C. Ultra-Rapid VOCs Sensors Based on Sparked-In_2O_3 Sensing Films. *Sens. Actuators, B* **2014**, *192*, 745–754.
(11) Li, X. L.; Lou, T. J.; Sun, X. M.; Li, Y. D. Highly Sensitive WO_3 Hollow-Sphere Gas Sensors. *Inorg. Chem.* **2004**, *43*, 5442–5449.
(12) Wang, L.; Teleki, A.; Pratsinis, S. E.; Gouma, P. I. Ferroelectric WO_3 Nanoparticles for Acetone Selective Detection. *Chem. Mater.* **2008**, *20*, 4794–4796.
(13) Dou, Z. F.; Cao, C. Y.; Chen, Y.; Song, W. G. Fabrication of Porous Co_3O_4 Nanowires with High CO Sensing Performance at a Low Operating Temperature. *Chem. Commun.* **2014**, *50*, 14889–14891.
(14) Liu, Y. Y.; Zhan, W. W.; He, Y.; Wang, Y. T.; Kong, X. J.; Kuang, Q.; Xie, Z. X.; Zheng, L. S. MOF-Templated Synthesis of Porous Co_3O_4 Concave Nanocubes with High Specific Surface Area and Their Gas Sensing Properties. *ACS Appl. Mater. Interfaces* **2014**, *6*, 4186–4195.
(15) Kim, H.-J.; Choi, K.-I.; Kim, K.-M.; Na, C. W.; Lee, J.-H. Highly Sensitive C_2H_5OH Sensors Using Fe-Doped NiO Hollow Spheres. *Sens. Actuators, B* **2012**, *171–172*, 1029–1037.
(16) Rai, P.; Yoon, J.-W.; Jeong, H.-M.; Hwang, S.-J.; Kwak, C.-H.; Lee, J.-H. Design of Highly Sensitive and Selective Au@NiO Yolk-Shell Nanoreactors for Gas Sensor Applications. *Nanoscale* **2014**, *6*, 8992–8999.
(17) Ahmad, S.; Jousseaume, B.; Servant, L.; Toupance, T.; Zakri, C. Self-Assembled Titanium-Based Hybrids with Cyclopentadienyl–Titanium Network Bonding. *Chem. Commun.* **2011**, *47*, 5001–5003.
(18) Zhang, L.; Zhao, D. Y.; Lou, X. W. Double-Shelled $CoMn_2O_4$ Hollow Microcubes as High-Capacity Anodes for Lithium-Ion Batteries. *Adv. Mater.* **2012**, *24*, 745–748.
(19) Li, J. F.; Wang, J. Z.; Liang, X.; Zhang, Z. J.; Liu, H. K.; Qian, Y. T.; Xiong, S. L. Hollow $MnCo_2O_4$ Submicrospheres with Multilevel Interiors: From Mesoporous Spheres to Yolk-in-Double-Shell Structures. *ACS Appl. Mater. Interfaces* **2014**, *6*, 24–30.
(20) Sun, P.; Zhou, X.; Wang, C.; Shimanoe, K.; Lu, G. Y.; Yamazoe, N. Hollow SnO_2/α-Fe_2O_3 Spheres with a Double-Shell Structure for Gas Sensors. *J. Mater. Chem. A* **2014**, *2*, 1302–1308.
(21) Ding, S. J.; Lou, X. W. SnO_2 Nanosheet Hollow Spheres with Improved Lithium Storage Capabilities. *Nanoscale* **2011**, *3*, 3586–3588.
(22) Li, L. L.; Chu, Y.; Liu, Y.; Dong, L. H. Template-Free Synthesis and Photocatalytic Properties of Novel Fe_2O_3 Hollow Spheres. *J. Phys. Chem. C* **2007**, *111*, 2123–2127.
(23) Wang, Z. Y.; Zhou, L.; Lou, X. W. Metal Oxide Hollow Nanostructures for Lithium-Ion Batteries. *Adv. Mater.* **2012**, *24*, 1903–1911.
(24) Guo, H.; Li, T. T.; Chen, W. W.; Liu, L. X.; Yang, X. J.; Wang, Y. P.; Guo, Y. C. General Design of Hollow Porous $CoFe_2O_4$ Nanocubes from Metal-Organic Frameworks with Extraordinary Lithium Storage. *Nanoscale* **2014**, *6*, 15168–15174.
(25) Liu, B.; Zeng, H. C. Symmetric and Asymmetric Ostwald Ripening in the Fabrication of Homogeneous Core-Shell Semiconductors. *Small* **2005**, *1*, 566–571.
(26) Yin, Y. D.; Rioux, R. M.; Erdonmez, C. K.; Hughes, S.; Somorjai, G. A.; Alivisatos, A. P. Formation of Hollow Nanocrystals Through the Nanoscale Kirkendall Effect. *Science* **2004**, *304*, 711–714.
(27) Tian, L.; Yang, X. F.; Lu, P.; Williams, L. D.; Wang, C. H.; Ou, S. Y.; Li, C. C.; Wu, M. M. Hollow Single-Crystal Spinel Nanocubes: The Case of Zinc Cobalt Oxide Grown by a Unique Kirkendall Effect. *Inorg. Chem.* **2008**, *47*, 5522–5524.
(28) Fan, H. J.; Gosele, U.; Zacharias, M. Formation of Nanotubes and Hollow Nanoparticles Based on Kirkendall and Diffusion Processes: A Review. *Small* **2007**, *3*, 1660–1671.
(29) Won, J. M.; Choi, S. H.; Hong, Y. J.; Ko, Y. N.; Kang, Y. C. Electrochemical Properties of Yolk-Shell Structured $ZnFe_2O_4$ Powders Prepared by a Simple Spray Drying Process as Anode Material for Lithium-Ion Battery. *Sci. Rep.* **2014**, *4*, 5857–5862.
(30) Shanmugavani, A.; Selvan, R. K. Synthesis of $ZnFe_2O_4$ Nanoparticles and Their Asymmetric Configuration with $Ni(OH)_2$ for a Pseudocapacitor. *RSC Adv.* **2014**, *4*, 27022–27029.
(31) Guo, P. Z.; Cui, L. J.; Wang, Y. Q.; Lv, M.; Wang, B. Y.; Zhao, X. S. Facile Synthesis of $ZnFe_2O_4$ Nanoparticles with Tunable Magnetic and Sensing Properties. *Langmuir* **2013**, *29*, 8997–9003.
(32) Liu, F.; Chu, X. F.; Dong, Y. P.; Zhang, W. B.; Sun, W. Q.; Shen, L. M. Acetone Gas Sensors Based on Graphene-$ZnFe_2O_4$ Composite Prepared by Solvothermal Method. *Sens. Actuators, B* **2013**, *188*, 469–474.
(33) Xing, Z.; Ju, Z. H.; Yang, J.; Xu, H. Y.; Qian, Y. T. One-Step Hydrothermal Synthesis of $ZnFe_2O_4$ Nano-Octahedrons as a High Capacity Anode Material for Li-Ion Batteries. *Nano Res.* **2012**, *5*, 477–485.
(34) Niu, X. S.; Du, W. P.; Du, W. M. Preparation and Gas Sensing Properties of ZnM_2O_4 (M = Fe, Co, Cr). *Sens. Actuators, B* **2004**, *99*, 405–409.

DOI: 10.1021/acsami.5b03537
ACS Appl. Mater. Interfaces 2015, 7, 15414–15421

(35) Reddy, C. V. G.; Manorama, S. V.; Rao, V. J. Preparation and Characterization of Ferrites As Gas Sensor Materials. *J. Mater. Sci. Lett.* **2000**, *19*, 775−778.
(36) Zhang, G. Y.; Li, C. S.; Cheng, F. Y.; Chen, J. $ZnFe_2O_4$ Tubes: Synthesis and Application to Gas Sensors with High Sensitivity and Low-Energy Consumption. *Sens. Actuators, B* **2007**, *120*, 403−410.
(37) Sun, P.; Zhao, W.; Cao, Y.; Guan, Y.; Sun, Y. F.; Lu, G. Y. Porous SnO_2 Hierarchical Nanosheets: Hydrothermal Preparation, Growth Mechanism, and Gas Sensing Properties. *CrystEngComm* **2011**, *13*, 3718−3724.
(38) Li, J. F.; Wang, J. Z.; Wexler, D.; Shi, D. Q.; Liang, J. W.; Liu, H. K.; Xiong, S. L.; Qian, Y. T. Simple Synthesis of Yolk-Shelled $ZnCo_2O_4$ Microspheres towards Enhancing the Electrochemical Performance of Lithium-Ion Batteries in Conjunction with a Sodium Carboxymethyl Cellulose Binder. *J. Mater. Chem. A* **2013**, *1*, 5596−5602.
(39) Qiu, Y. C.; Yang, S. H.; Deng, H.; Jin, L. M.; Li, W. S. A Novel Nanostructured Spinel $ZnCo_2O_4$ Electrode Material: Morphology Conserved Transformation from a Hexagonal Shaped Nanodisk Precursor and Application in Lithium Ion Batteries. *J. Mater. Chem.* **2010**, *20*, 4439−4444.
(40) Wang, X.; Wu, X. L.; Guo, Y. G.; Zhong, Y. T.; Cao, X. Q.; Ma, Y.; Yao, J. N. Synthesis and Lithium Storage Properties of Co_3O_4 Nanosheet-Assembled Multishelled Hollow Spheres. *Adv. Funct. Mater.* **2010**, *20*, 1680−1686.
(41) Hou, L. R.; Lian, L.; Zhang, L. H.; Pang, G.; Yuan, C. Z.; Zhang, X. G. Self-Sacrifice Template Fabrication of Hierarchical Mesoporous Bi-Component-Active $ZnO/ZnFe_2O_4$ Sub-Microcubes as Superior Anode Towards High-Performance Lithium-Ion Battery. *Adv. Funct. Mater.* **2015**, *25*, 238−246.
(42) Lv, H. J.; Ma, L.; Zeng, P.; Ke, D. N.; Peng, T. Y. Synthesis of Floriated $ZnFe_2O_4$ with Porous Nanorod Structures and Its Photocatalytic Hydrogen Production under Visible Light. *J. Mater. Chem.* **2010**, *20*, 3665−3672.
(43) Wang, M.; Ai, Z. H.; Zhang, L. L. Generalized Preparation of Porous Nanocrystalline $ZnFe_2O_4$ Superstructures from Zinc Ferrioxalate Precursor and Its Superparamagnetic Property. *J. Phys. Chem. C* **2008**, *112*, 13163−13169.
(44) Wang, S. R.; Zhang, J. X.; Yang, J. D.; Gao, X. L.; Zhang, H. X.; Wang, Y. S.; Zhu, Z. Y. Spinel $ZnFe_2O_4$ Nanoparticle-Decorated Rod-Like ZnO Nanoheterostructures for Enhanced Gas Sensing Performances. *RSC Adv.* **2015**, *5*, 10048−10057.
(45) Andreeva, D.; Tabakova, T.; Idakiev, V.; Christov, P.; Giovanoli, R. Au/α-Fe_2O_3 Catalyst for Water-Gas Shift Reaction Prepared by Peposition-Precipitation. *Appl. Catal., A* **1998**, *169*, 9−14.
(46) Hu, D.; Han, B. Q.; Deng, S. J.; Feng, Z. P.; Wang, Y.; Popovic, J.; Nuskol, M.; Wang, Y. D.; Djerdj, I. Novel Mixed Phase SnO_2 Nanorods Assembled with SnO_2 Nanocrystals for Enhancing Gas-Sensing Performance toward Isopropanol Gas. *J. Phys. Chem. C* **2014**, *118*, 9832−9840.
(47) Li, L. L.; Cheah, Y. L.; Ko, Y.; Teh, P. F.; Wee, G.; Wong, C. L.; Peng, S. J.; Srinivasan, M. The Facile Synthesis of Hierarchical Porous Flower-like $NiCo_2O_4$ with Superior Lithium Storage Properties. *J. Mater. Chem. A* **2013**, *1*, 10935−10941.
(48) Neri, G.; Bonavita, A.; Micali, G.; Rizzo, G.; Callone, E.; Carturan, G. Resistive CO Gas Sensors Based on In_2O_3 and $InSnO_x$ Nanopowders Synthesized via Starch-Aided Sol−Gel Process for Automotive Applications. *Sens. Actuators, B* **2008**, *132*, 224−233.
(49) Zhou, X.; Liu, J. Y.; Wang, C.; Sun, P.; Hu, X. L.; Li, X. W.; Shimanoe, K.; Yamazoe, N.; Lu, G. Y. Highly Sensitive Acetone Gas Sensor Based on Porous $ZnFe_2O_4$ Nanospheres. *Sens. Actuators, B* **2015**, *6*, 577−583.
(50) Zhou, X.; Feng, W.; Wang, C.; Hu, X. L.; Li, X. W.; Sun, P.; Shimanoe, K.; Yamazoe, N.; Lu, G. Y. Porous $ZnO/ZnCo_2O_4$ Hollow Spheres: Synthesis, Characterization, and Applications in Gas Sensing. *J. Mater. Chem. A* **2014**, *2*, 17683−17690.
(51) Zen, W.; Liu, T. M. Gas-Sensing Properties of SnO_2−TiO_2-Based Sensor for Volatile Organic Compound Gas and Its Sensing Mechanism. *Phys. B* **2010**, *405*, 1345−1348.
(52) Yamazoe, N.; Sakai, G.; Shimanoe, K. Oxide Semiconductor Gas Sensors. *Catal. Surv. Asia* **2003**, *7*, 63−75.
(53) Park, S. H.; An, S. Y.; Mun, Y. H.; Lee, C. M. UV-Enhanced NO_2 Gas Sensing Properties of SnO_2-Core/ZnO-Shell Nanowires at Room Temperature. *ACS Appl. Mater. Interfaces* **2013**, *5*, 4285−4292.
(54) Liu, X. J.; Chang, Z.; Luo, L.; Lei, X. D.; Liu, J. F.; Sun, X. M. Sea Urchin-like Ag-α-Fe_2O_3 Nanocomposite Microspheres: Synthesis and Gas Sensing Applications. *J. Mater. Chem.* **2012**, *22*, 7232−7238.
(55) Yamazoe, N. New Approach for Improving Semiconductor Gas Sensors. *Sens. Actuators, B* **1991**, *5*, 7−19.

DOI: 10.1021/acsami.5b03537
ACS Appl. Mater. Interfaces 2015, 7, 15414−15421